Insights into ENSO Diversity from an Intermediate Coupled Model. Part I: Uniqueness and Sensitivity of the ENSO Mode

LICHENG GENG[a] AND FEI-FEI JIN[a]

[a] *Department of Atmospheric Sciences, School of Ocean and Earth Science and Technology, Honolulu, Hawaii*

(Manuscript received 22 January 2023, in final form 3 June 2023, accepted 26 July 2023)

ABSTRACT: The basic dynamics of the spatiotemporal diversity for El Niño–Southern Oscillation (ENSO) has been the subject of extensive research and, while several hypotheses have been proposed, remains elusive. One promising line of studies suggests that the observed eastern Pacific (EP) and central Pacific (CP) ENSO may originate from two coexisting leading ENSO modes. We show that the coexistence of unstable EP-like and CP-like modes in these studies arises from contaminated linear stability analysis due to unnoticed numerical scheme caveats. In this two-part study, we further investigate the dynamics of ENSO diversity within a Cane–Zebiak-type model. We first revisit the linear stability issue to demonstrate that only one ENSO-like linear leading mode exists under realistic climate conditions. This single leading ENSO mode can be linked to either a coupled recharge-oscillator (RO) mode favored by the thermocline feedback or a wave-oscillator (WO) mode favored by the zonal advective feedback at the weak air–sea coupling end. Strong competition between the RO and WO modes for their prominence in shaping this ENSO mode into a generalized RO mode makes it sensitive to moderate changes in these two key feedbacks. Modulations of climate conditions yield corresponding modulations in spatial pattern, amplitude, and period associated with this ENSO mode. However, the ENSO behavior undergoing this linear climate condition modulations alone does not seem consistent with the observed ENSO diversity, suggesting the inadequacy of linear dynamics in explaining ENSO diversity. A nonlinear mechanism for ENSO diversity will be proposed and discussed in Part II.

KEYWORDS: ENSO; Idealized models; Stability

1. Introduction

El Niño–Southern Oscillation (ENSO), featuring basin-scale interaction between the tropical Pacific atmosphere and ocean on the interannual time scale, has been a subject of active research due to its profound impact. The discovery of significant interevent spatiotemporal diversity initiated a new line of research on ENSO in the last two decades. Although the classification of ENSO events remains in debate (e.g., Giese and Ray 2011; Johnson 2013), it is generally acknowledged that El Niño can be roughly categorized into the eastern Pacific (EP)-type and central Pacific (CP)-type according to the location of sea surface temperature anomaly (SSTA) maxima during the mature phase (Larkin and Harrison 2005; Ashok et al. 2007; Kug et al. 2009; Kao and Yu 2009; Yeh et al. 2009). On the other hand, La Niña exhibits less pattern diversity (Kug and Ham 2011; Taschetto et al. 2014).

Physical processes associated with the two types of El Niño are well documented. Heat budget analysis indicates that the two types of El Niño develop under different combinations of the thermocline feedback and zonal advective feedback, with the former (latter) playing a dominant role in the growth of SSTA during EP (CP) El Niño (Kug et al. 2009; Capotondi 2013). The oceanic delayed-negative feedback contributing to ENSO's phase transition also differs between the two types of El Niño. The heat content discharge/recharge plays a crucial role in transitions between EP El Niño and La Niña (Jin 1997a,b; Meinen and McPhaden 2000) but is less distinctive for CP El Niño (Kug et al. 2010; McPhaden 2012; Capotondi 2013; Ren and Jin 2013). Consequently, EP El Niño is typically followed by a transition into La Niña (Dommenget et al. 2013), whereas CP El Niño is generally more episodic-like, exhibiting less apparent phase reversal.

A linear mechanism from the perspective of potential ENSO-like normal modes has been put forth toward understanding the coexistence of the two types of El Niño. Bejarano and Jin (2008) and Xie and Jin (2018), which will be referred to collectively as BXJ hereafter, identified two coexisting ENSO-like leading oscillatory eigenmodes through linear stability analysis using the Cane–Zebiak (CZ) model (Zebiak and Cane 1987). These two eigenmodes exhibit spatial and temporal characteristics resembling those associated with observed EP and CP El Niño, respectively. BXJ interpreted the two types of El Niño, together with corresponding La Niña, as two natural oscillations with distinct linear dynamics. On the other hand, an earlier study by Fedorov and Philander (2001), which performed similar linear stability analyses but with a stripped-down version of the CZ model, suggested the existence of a single leading ENSO-like mode. The stripped-down version of the CZ model simplifies the SST equation by assuming a prescribed meridional profile of SSTA, but the essential dynamic and thermodynamic processes relevant to ENSO remain unchanged. The ENSO-like mode shows high sensitivity to the prescribed basic state and is generally categorized into two distinct families featuring either EP or CP El Niño–like characteristics. The seeming contradiction between BXJ and Fedorov and Philander (2001) was not settled until our recent finding that, as will be discussed in the next section, the linear stability analysis in BXJ suffers from some caveats in its numerical

Corresponding author: Fei-Fei Jin, jff@hawaii.edu

DOI: 10.1175/JCLI-D-23-0043.1

schemes. The erroneous calculation thereby casts doubt on the relevance of the two coexisting leading ENSO modes and calls for a reinterpretation of ENSO diversity identified in long-term simulations.

An alternative linear mechanism for ENSO diversity speculates that the two types of El Niño take place through distinct nonmodal transient growths from their respective preceding optimal initial perturbations (Newman et al. 2011a,b; Vimont et al. 2014, 2022; Capotondi and Sardeshmukh 2015). Note that the optimal initial perturbations along this line of study are obtained by analyzing the governing linear operator derived from the data-driven linear inverse modeling (LIM) approach. Not surprisingly, they show significant sensitivity to the formulation of the LIM, such as the choice of independent variables (Newman et al. 2011b; Capotondi and Sardeshmukh 2015) and whether seasonality is taken into consideration (Shin et al. 2021; Vimont et al. 2022). Another issue with this mechanism is whether the optimal initial perturbations can be efficiently excited has not been thoroughly tested. Newman et al. (2011a) performed a linear stochastic simulation and suggested that two types of El Niño can be stochastically driven by noise forcing. In their study, both the linear operator and the noise forcing are derived from LIM. However, as the effects of nonlinear processes were implicitly included in the linear operator and statistics of noise forcing obtained with LIM, whether realistic climate variabilities can project onto the optimal initial perturbations and then lead to the two types of El Niño deserves further investigation.

In recent years, physical processes beyond those depicted by the linear dynamics, including atmospheric/oceanic nonlinear processes and scale-interaction processes, are widely acknowledged to contribute to ENSO diversity. The nonlinearity effect is evidenced by noticing that the observed ENSO events can be classified into strong and moderate regimes (Takahashi et al. 2011). Extreme EP El Niño (e.g., the 1982/83 and 1997/98 events) typically resides in the strong regime, whereas the moderate regime incorporates CP El Niño, weak EP El Niño, and La Niña. Convective heating nonlinearity, which acts as a switch for extreme EP El Niño because a substantial warm SSTA is required to excite deep convection in the eastern Pacific, serves as a key candidate for the sources of nonlinearity (Takahashi and Dewitte 2016; Williams and Patricola 2018; Okumura 2019). The effect of the scale-interaction processes on ENSO diversity is evidenced by the essential role played by the westerly wind burst (WWB) events in the emergence of irregular occurrences of EP and CP El Niño in numerical simulations (Chen et al. 2015; Chen and Majda 2017; Hayashi and Watanabe 2017; Chen et al. 2018; Yang et al. 2021). Whether a WWB leads to EP or CP El Niño is suggested to depend on its interplay with ocean preconditions (Lian et al. 2014; Fedorov et al. 2015; Jadhav et al. 2015; Hu and Fedorov 2019). On the other hand, ENSO's modulation of WWB adds to the atmospheric nonlinearity and thereby favors ENSO diversity.

Despite the success of the above mechanisms in explaining aspects of ENSO diversity, whether they constitute a comprehensive picture of understanding ENSO diversity remains unclear. From the authors' knowledge, the relative contribution from these mechanisms has not been thoroughly tested, possibly due to the intertwining of various mechanisms in previous studies. A comprehensive framework that allows a clean separation of potential mechanisms is needed to disentangle the basic dynamics of ENSO diversity unambiguously. Recently, Geng and Jin (2022, hereafter GJ22) proposed a revised CZ model, referred to as RCZ, which simulates ENSO diversity to a satisfactory extent. This model serves as an elegant tool for studying ENSO diversity by virtue of the facts that (i) the simple CZ-type framework allows straightforward identification of the ENSO mode(s), and (ii) most of the relevant physical processes for ENSO diversity proposed in earlier studies have been explicitly built in. In this two-part study, we aim to provide a general understanding of the basic dynamics of ENSO diversity. In Part I, we will re-examine the linear ENSO dynamics with an emphasis on (i) whether there indeed exists a single leading ENSO mode and (ii) if so, what determines the uniqueness of the ENSO mode. Part II (Geng and Jin 2023, hereafter Part II) will primarily focus on the pathway from the ENSO mode(s) to the coexistence of the two types of El Niño.

This paper begins with a discussion on the coding issues in BXJ and the updated ENSO mode after error correction in section 2. The linear ENSO dynamics is then more deeply investigated via linear stability analysis with RCZ. A brief introduction to RCZ and the procedures of linear stability analysis are provided in section 3. In section 4, we present the existence of a single leading ENSO mode under the observed climate condition and discuss its properties. In section 5, the dynamics of the ENSO mode, especially the mechanism for its uniqueness, is investigated by exploring the ENSO mode properties in broad parameter spaces. The ENSO mode's sensitivity will be discussed as well. Discussions on the relevance of some other potential linear mechanisms of ENSO diversity proposed in previous studies are provided in section 6, followed by a summary in section 7.

2. Revisiting coexisting leading ENSO modes in previous studies

Early theoretical studies speculate ENSO as a natural oscillator and investigate basic ENSO dynamics by examining properties of the most unstable atmosphere–ocean coupled mode (e.g., Hirst 1986; Rennick and Haney 1986; Battisti and Hirst 1989; Wakata and Sarachik 1991). A logical follow-up question is this: Are there two ENSO-like modes of relevance for the two types of El Niño? BXJ tested this hypothesis by performing a series of linear stability analyses of the CZ model in a broad two-dimensional basic state space spanned by varying prescribed mean wind stress intensity and reference upper-layer depth. The existence of two groups of ENSO-like linear modes in the basic state space was identified. With certain sets of the prescribed basic state, both these two modes are unstable and dominate over the rest oscillatory modes.

Here, we reproduce BXJ's linear stability analysis with a series of basic states in which the reference upper layer is of a fixed depth at 140 m and the relative mean wind stress

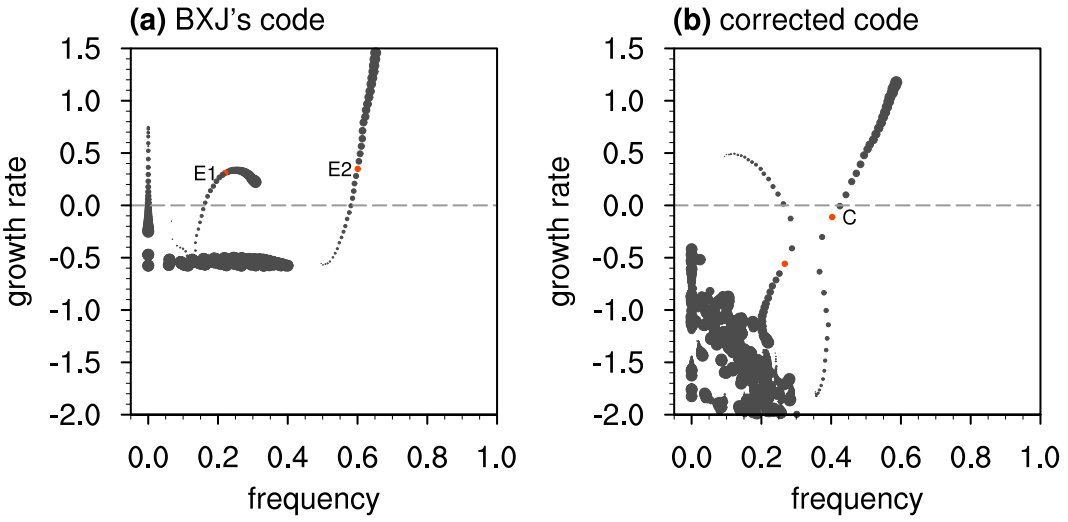

FIG. 1. Growth rate (yr^{-1}) and frequency (yr^{-1}) of the CZ model's eigenmodes calculated from (a) BXJ's code and (b) the corrected code. The eigenmodes are obtained with a series of basic states in which the reference upper layer is 140 m and the relative mean wind stress intensity ranges from 80% to 120% with an increment of 1%. The size of the dots increases with stronger mean wind stress. The red dots denote the two leading oscillatory modes obtained with the basic state of which the relative mean wind stress intensity is 100%. In (a), the two leading oscillatory modes are labeled as E1 and E2. In (b), the first leading oscillatory mode is labeled as C.

intensity varies continuously from 80% to 120%. The relative mean wind stress intensity being larger (smaller) than 100% corresponds to a more El Niño (La Niña)–like basic state compared with the observations. Figure 1a shows the growth rate and frequency of the eigenmodes in this basic state space. Consistent with BXJ, two coexisting groups of oscillatory eigenmodes are clearly identified. These two groups of eigenmodes exhibit contrasting frequencies: one with a period of about 4 years and the other slightly shorter than 2 years. With stronger mean wind stress, these two modes generally see a larger growth rate, except that the EP mode gradually saturates and becomes less unstable. With a basic state closest to the observations (i.e., the relative mean wind stress intensity being 100%), these two modes, denoted by red dots in Fig. 1a, are both unstable. The corresponding SSTA patterns during the warm peak phase are shown in Figs. 2a and 2b. The slow and fast eigenmodes exhibit SSTA maxima in the eastern and central Pacific and are thus referred to as EP and CP modes by BXJ, respectively. In addition to the EP and CP modes, there is also a group of stationary modes, which can be identified in Bejarano and Jin (2008) as well. Figure 1a is generally comparable with Fig. 2c in Bejarano and Jin (2008). The slight difference between them results from the fact that the model parameters utilized in BXJ are not fully recovered.

The linear dynamical operator for the above stability analysis, a two-dimensional matrix, is obtained via the perturbation method. Technically, the state variables are perturbed with a small-amplitude coefficient grid by grid and variable by variable. At each perturbation, the rest of the state variables that are not perturbed are assigned a zero value. The tendency of all state variables induced by each perturbation then constitutes a column of the matrix. In BXJ, these tendencies are calculated via integrating the CZ model one time step forward and then taking the subtraction between the state variables at these two timesteps. Upon attempts to reproduce BXJ's results, we uncovered that they made a critical coding error in calculating the anomalous horizontal and vertical temperature advection terms. Corresponding to the nth perturbation, the anomalous horizontal advection is calculated as $F^n_{\text{adv}} = -\mathbf{U}^{n-1} \cdot \nabla \overline{T}$. Here, $\overline{T}$ is the prescribed mean SST, and $\mathbf{U}^{n-1}$ is the anomalous surface current associated with the $n-1$th perturbation. Apparently, there is a mismatch between the perturbation and temperature tendency, and F^n_{adv} does not represent the true tendency induced by the nth perturbation. To correct this error, F^n_{adv} shall be calculated as $F^n_{\text{adv}} = -\mathbf{U}^n \cdot \nabla \overline{T}$, where $\mathbf{U}^n$ denotes the anomalous surface current associated with the nth perturbation. A similar correction shall also be made toward the calculation of anomalous vertical advection to ensure that the anomalous subsurface temperature is diagnosed from the thermocline fluctuation associated with the nth perturbation.

Apart from the above critical coding error, there are two additional minor issues with BXJ, making their linear stability analysis less accurate. First, as mentioned above, the tendency terms of the state variables are obtained by integrating the model one step forward. Note that an implicit time-integration scheme is utilized in the CZ model. As a result, the tendency terms are dependent on the numerical time step. A more appropriate way to perform linear stability analysis would be to instantaneously diagnose the tendency terms corresponding to each perturbation without integrating one step forward. The second issue with BXJ is associated with the inappropriate use of the upwind finite-difference scheme for horizontal temperature advection. The sign of the surface current determines whether the forward or backward finite-difference is utilized. For example, the mean zonal advection $(\overline{u}\partial_x T)_k$ is written as $\overline{u}_k[(T_k - T_{k-1})/\Delta x]$ for a positive $\overline{u}_k$ and

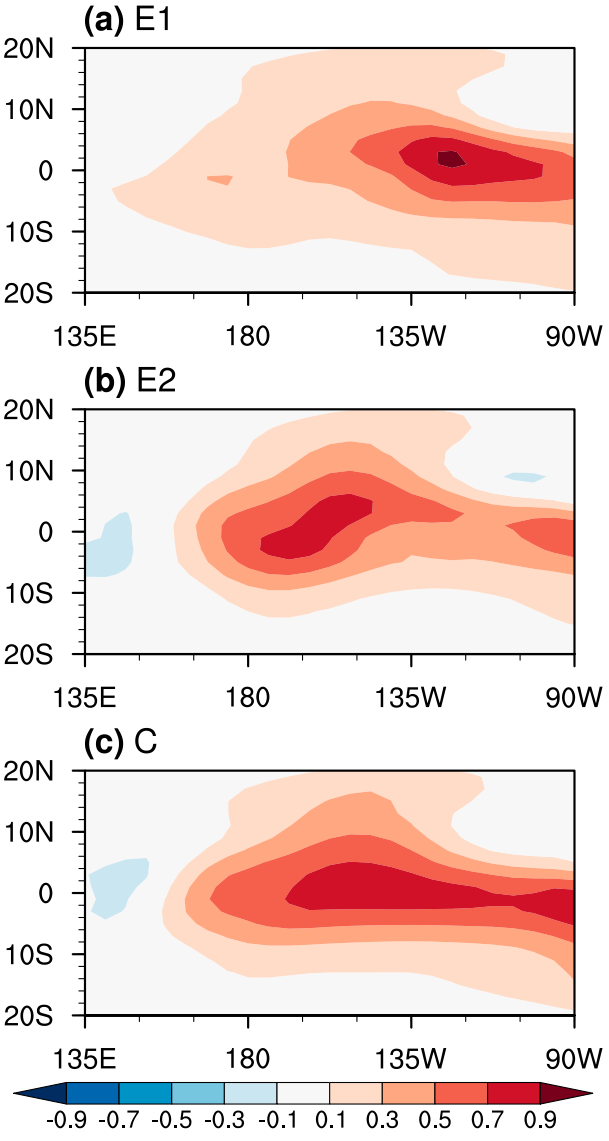

FIG. 2. (a), (b) SSTA pattern during the warm peak phase of the eigenmodes labeled with E1 and E2 in Fig. 1a. (c) As in (a), but for the eigenmode labeled with C in Fig. 1b.

$\overline{u}_k[(T_{k+1} - T_k)/\Delta x]$ for a negative $\overline{u}_k$. Similarly, the anomalous zonal advection $(u\partial_x\overline{T})_k$ is written as $u_k[(\overline{T}_k - \overline{T}_{k-1})/\Delta x]$ for a positive u_k and $u_k[(\overline{T}_{k+1} - \overline{T}_k)/\Delta x]$ for a negative u_k. Here, subscript $k-1$, k, and $k+1$ represent three adjacent grids in the zonal direction, and Δx is the zonal grid space. Variables with and without an overbar represent the mean and anomalous field, respectively. It is clear that different finite-difference schemes (i.e., forward vs backward) may be used between the mean and anomalous zonal advection on the same grid, which is not quite physically meaningful. Such a scheme also introduces artificial sensitivity of the stability analysis to the perturbation coefficient. A positive or negative perturbation in the zonal surface current leads to different choices of the finite-difference scheme. An easy way to avoid these two shortcomings is to determine whether a forward or backward finite-difference scheme should be used according to the sign of the total zonal surface current $\overline{u}_k + u_k$ when calculating both the mean and anomalous zonal temperature advection. By doing so, the artificial sensitivity to the perturbation coefficient is removed because the perturbed zonal surface current anomaly is typically several orders smaller than the mean current.

After correcting these coding issues, a series of linear stability analyses similar to the above are performed. Although there still exist two groups of eigenmodes with distinct frequencies, these two groups of eigenmodes cannot be both unstable (Fig. 1b). With stronger mean wind stress, the lower-frequency (higher-frequency) mode becomes more damped (unstable). When the relative mean wind stress intensity is stronger than 100%, the first leading mode is unstable, whereas the second leading oscillatory mode is strongly stable. Consequently, there exists a single unstable oscillatory mode for any prescribed basic state. Figure 2c shows the SSTA pattern at the peak phase of the leading oscillatory mode associated with the basic state closest to the observations (i.e., the relative mean wind stress intensity being 100%). It features broad warm SSTA over the central-eastern Pacific and is thus mixed CP/EP-like. The stationary mode identified in BXJ is eliminated with the corrected code, indicating that it was introduced by the corrupted dynamical linear operator.

It needs to be pointed out that the error in BXJ's linear stability analysis does not invalidate their finding that ENSO diversity can be simulated with the CZ model. However, instead of being attributed to the coexisting leading ENSO modes as in BXJ, the mechanism of such ENSO diversity needs to be reinterpreted.

3. Model and methodology

a. *Model description of RCZ*

The classic CZ model provides a simple but comprehensive framework for studying ENSO theory. In a recent study, GJ22 uncovered some caveats in the CZ model components by performing uncoupled simulations with observed external forcings. Inspired by that, they further revised the CZ model by modifying some key parameterization schemes including, but not limited to, the formulation of diabatic heating anomaly response to SSTA and the subsurface temperature anomaly response to thermocline fluctuation. A stochastic parameterization scheme for WWB has been implemented as well to capture the stochastic forcing. This revised model, RCZ, reasonably simulates observed ENSO characteristics (e.g., spatial pattern, phase locking, El Niño/La Niña asymmetry, and ENSO diversity). In this two-part study, RCZ serves as the tool for studying the dynamics of ENSO diversity. Compared with that proposed in GJ22, a few minor modifications are made to the model formulation. The anomalous meridional advection is reduced to remove the overly strong poleward extension of SSTA along the eastern boundary. In addition, a few coefficients in the parameterization schemes are slightly modified. These modifications have a negligible impact on the

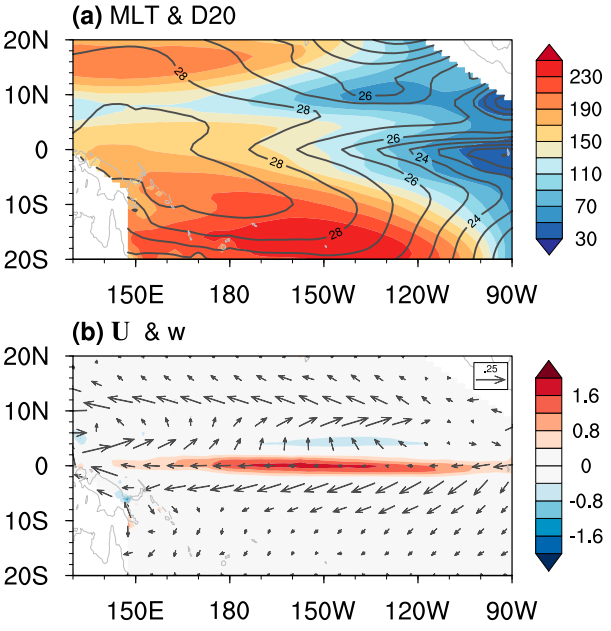

FIG. 3. The prescribed basic state for the linear stability analysis. (a) Mixed layer temperature (MLT; contour; °C) and thermocline depth (shaded; m). (b) Mixed layer ocean current (vector; m s^{-1}) and upwelling velocity at the base of the mixed layer (shaded; m day^{-1}).

ENSO features presented in GJ22. The prescribed basic state of RCZ is obtained from the long-term climatology (averaged between 1980 and 2014) of the ensemble average of multiple reanalysis datasets. More detailed data descriptions can be found in Table 1 of GJ22. Similar to previous studies on the linear ENSO dynamics (e.g., BXJ; Fedorov and Philander 2001), most of the analysis in Part I is performed with an annual mean basic state. As shown in Fig. 3, this prescribed basic state features a strong zonal temperature gradient in the central Pacific, a deep (shallow) thermocline measured by the depth of the 20°C-isotherm in the western (eastern) tropical Pacific, and strong upwelling along the equatorial Pacific with its peak in the central Pacific.

b. *Linear stability analysis*

Following previous studies on ENSO theory, a linear stability analysis of RCZ based on the perturbation method is utilized to investigate the linear ENSO dynamics. To ensure linearity of the stability analysis, each element of the state variables is perturbed by both a positive and negative small-amplitude coefficient (i.e., 10^{-3} for mixed layer temperature and 10^{-5} for ocean dynamics variables), and the average of the positive and negative perturbation-induced tendency of the state variables constitute one column of the linear dynamical operator. The ENSO mode is identified as the leading eigenmode on the interannual time scale.

To investigate how the ENSO mode emerges from the uncoupled SST mode and ocean dynamics mode as a result of air–sea coupling, the properties of the ENSO mode are systematically examined through a series of linear stability analyses in which the dynamical air–sea coupling strength and intensity of thermodynamic feedback processes vary within a broad but reasonable range. Technically, the air–sea coupling strength is controlled by a nondimensional dynamical coupling coefficient, denoted as μ. This coefficient is introduced in the parameterization of SSTA-determined diabatic heating anomaly in the form of $\dot{Q}_a = \mu a_Q \exp(b_Q \overline{T})\{b_Q T + (1/2)[b_Q M(T)]^2 + (1/6)[b_Q M(T)]^3\}$, where $\dot{Q}_a$ is the diabatic heating anomaly, $\overline{T}$ and T denote the prescribed mean SST and SSTA, respectively, a_Q and b_Q are empirically determined from the observations, and $M(T)$ is the smoothed Heaviside function defined as $M(t) = 0.5T[\tanh(T/T_0) + 1]$ with $T_0 = 1$°C. Physically, μ controls the intensity of wind stress response to a unit of SSTA. Its default value of 1 corresponds to the situation where the atmospheric model-simulated surface wind stress response to observed SSTA is most realistic against observations. As μ approaches zero, the air–sea coupling is switched off because SSTA has no effect on the surface wind stress. By investigating how the ENSO mode varies with μ, it is possible to trace its dynamical origin rooted in the uncoupled ocean dynamics. In addition, varying μ mimics the process where an El Niño (La Niña)–like mean SST change associated with a weakened (strengthened) mean wind stress amplifies (reduces) the amplitude of wind stress response to a unit of SSTA (Bayr and Latif 2023). Thus, investigating the sensitivity of the ENSO mode properties at μ around 1 allows us to explore how the ENSO mode may respond to a changing climate.

To further examine its dynamics and sensitivity, the ENSO mode is investigated in the parameter space spanned by varying intensities of thermodynamic feedback processes, including the thermocline feedback, zonal advective feedback, and Ekman feedback. The nondimensional parameters controlling the intensities of these feedbacks, namely γ_{TH}, γ_{ZA}, and γ_{EK}, are introduced in the mixed-layer temperature equation as

$$\partial_t T_m = \gamma_{TH}\overline{w}\frac{T_{sub}}{H} - \gamma_{ZA}u\partial_x\overline{T}_m - \gamma_{EK}(w\overline{T}_z + v\partial_y\overline{T}_m) - \left(\overline{u}\partial_x T_m + \overline{v}\partial_y T_m + \overline{w}\frac{T_m}{H}\right) - \alpha T_m. \quad (1)$$

Here, T_m, T_{sub}, u, v, and w are the mixed layer temperature, subsurface temperature at a fixed depth H (75 m), zonal ocean current, meridional current, and upwelling at the bottom of the mixed layer, respectively. Variables with an overbar denote the prescribed basic state, whereas those without an overbar correspond to anomalous fields. The first three terms on the right-hand side of Eq. (1) denote the thermocline feedback, zonal advective feedback, and Ekman feedback, respectively. The Ekman feedback term incorporates both the anomalous vertical and meridional advection terms, in which the former is dominant. The intensity of these three feedbacks is controlled by the nondimensional parameters γ_{TH}, γ_{ZA}, and γ_{EK}, of which the default value is 1. The other two terms denote the mean advection of anomalous temperature and Newtonian cooling.

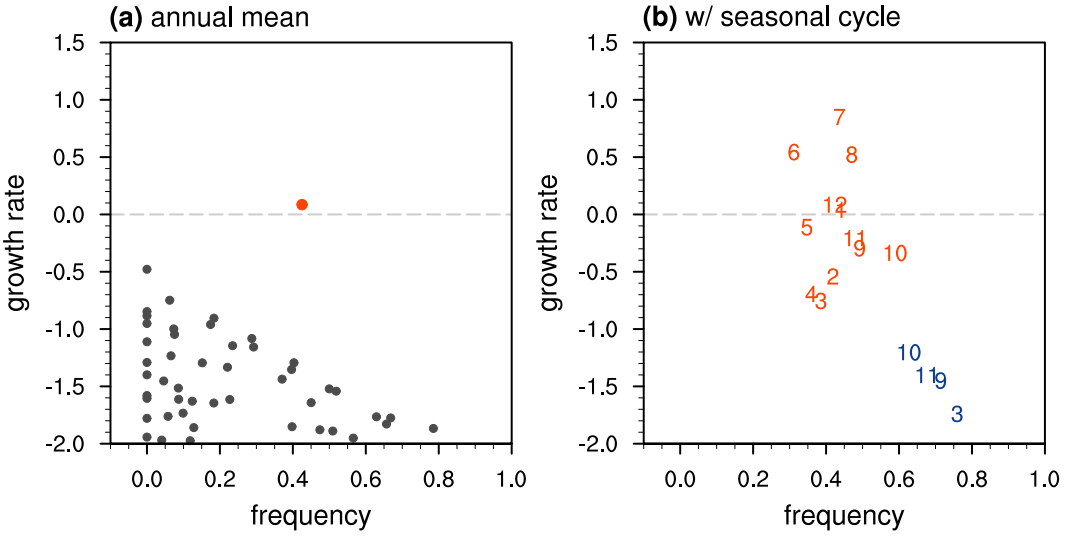

FIG. 4. (a) Growth rate (yr^{-1}) and frequency (yr^{-1}) of the eigenmodes of RCZ with an annual mean basic state. The first leading mode (i.e., ENSO mode) is denoted by the red dot. (b) Growth rate and frequency of the first (red label) and second (blue label) leading modes that are distinguishable from the uncoupled modes. These modes are obtained with the prescribed basic state in each of the 12 calendar months. The numbers in color denote the corresponding calendar month of the basic state.

4. A single leading ENSO mode under the observed climate condition

With the default model setting (i.e., $\mu = 1$, $\gamma_{TH} = 1$, $\gamma_{ZA} = 1$, $\gamma_{EK} = 1$) corresponding to the observed climate condition, the scatterplot of RCZ's eigenmodes clearly demonstrates the existence of a single leading oscillatory mode as denoted by the red dot in Fig. 4a. This mode, referred to as the ENSO mode, is at near-neutrality with a near-zero growth rate and has a frequency (period) of 0.45 yr^{-1} (about 2 years). Figure 5 shows the spatial pattern of SSTA and the thermocline fluctuation associated with the ENSO mode at various stages during its life cycle. At the warm peak phase, the warm SSTA spans broadly over the tropical Pacific and exhibits maximum SSTA over the central-eastern Pacific (Fig. 5b). This indicates that the ENSO mode is more-or-less mixed CP/EP-like. A similar SSTA pattern broadly spanning over the tropical Pacific can also be found with the leading oscillatory mode *C* in Fig. 2c. Consistent with the equatorial Sverdrup balance approximation, the warm SSTA and its induced eastward zonal wind stress anomaly in the central Pacific are accompanied by a shoaled (deepened) thermocline over the eastern (western) Pacific. The cold peak phase sees identical patterns but with opposite signs (Fig. 5d). As the cold and warm phases shift to opposite phases, the integrated equatorial thermocline deepens and shoals, respectively (Figs. 5a,c). This is consistent with the discharge/recharge paradigm (Jin 1997a), in which recharge (discharge) of the equatorial ocean heat content precedes the emergence of warm (cold) SSTA. The above ENSO mode spatial characteristics (i.e., SSTA maxima in the central-eastern Pacific at the peak phases and ocean heat content discharge/recharge at the transition phases) are also generally consistent with those associated with the observed ENSO cycle, which is identified through a lead–lag linear regression against the observed Niño-3.4 index (not shown). The primary difference between the ENSO mode and the observed ENSO cycle is reflected in the ENSO mode's small meridional scale of SSTA. In addition, the tropical thermocline fluctuation at the transition phases of the ENSO mode is more narrowly confined within the deep tropics compared with the observations. The reason for this smaller-than-observed meridional scale needs to be further examined.

The time evolution of the equatorial (5°S–5°N average) SSTA and heat budget terms associated with the ENSO mode are shown in Fig. 6. The mean advection term, along with the Newtonian cooling term, contributes to the damping of SSTA (Fig. 6a). The thermocline feedback, which is in phase with SSTA in the eastern Pacific, primarily maintains SSTA against the damping terms (Fig. 6b). Note that the thermocline feedback associated with the zonal mean component of the thermocline fluctuation is in quadrature with SSTA in time evolution. This is consistent with the discharge/recharge paradigm that zonal mean thermocline fluctuation leads to ENSO's phase transition. The zonal advective feedback centers over the central Pacific and leads SSTA by a phase of less than a quarter of the ENSO mode's period, thus contributing to the phase transition and growth of SSTA (Fig. 6c). Its amplitude is similar to the thermocline feedback associated with the zonal mean thermocline fluctuation. The Ekman feedback, which exhibits a smaller amplitude than the other two feedbacks, serves to maintain SSTA in the central Pacific (Fig. 6d).

The uniqueness of the ENSO mode is found not only with the annual mean basic state but also with the basic state from each of the 12 calendar months (Fig. 4b). There is at most one leading mode dominating over the uncoupled modes (i.e., the black dots in Fig. 4a) at each calendar month. Although a

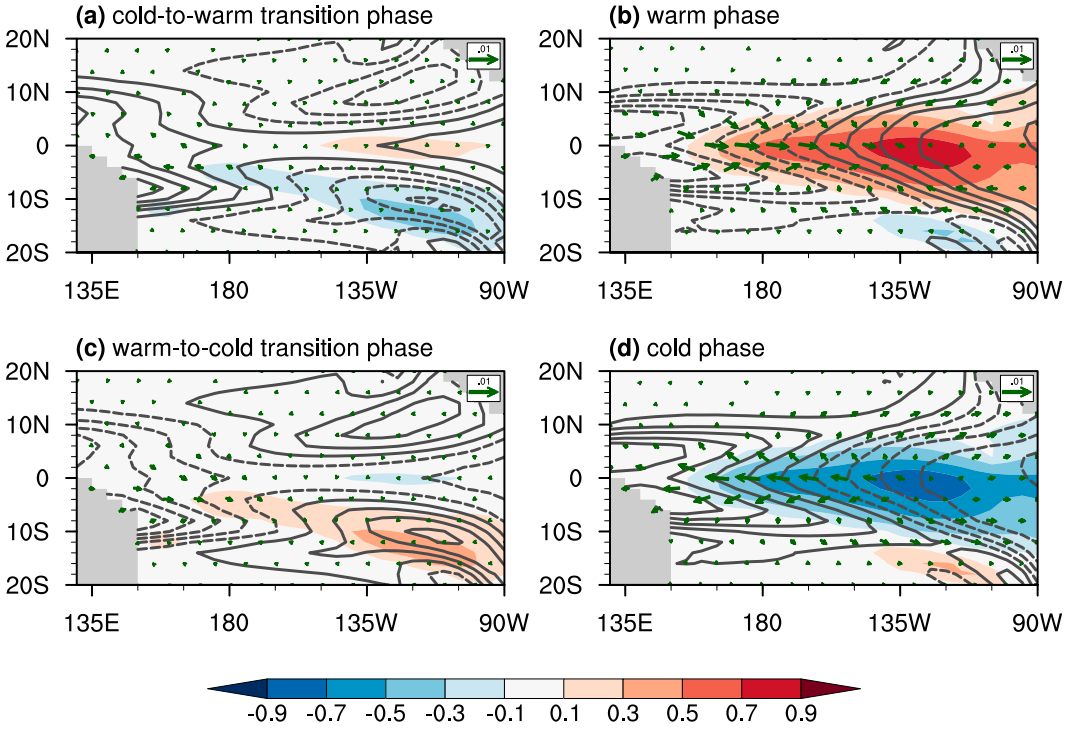

FIG. 5. Spatial pattern of SSTA (shaded; °C), thermocline fluctuation (contour; m), and anomalous surface wind stress (vector; N m^{-2}) associated with the ENSO mode at its (a) cold-to-warm transition phase, (b) warm peak phase, (c) warm-to-cold transition phase, and (d) cold peak phase. The contour level for thermocline fluctuation is 2 m, and dashed contours denote shoaling of the thermocline.

second coupled oscillatory mode can be identified in boreal spring and autumn, its growth rate is smaller than -1 $month^{-1}$ and thus may not play a significant role in the linear ENSO dynamics. The growth rate of the first leading mode (i.e., ENSO mode) peaks at the end of boreal summer. This is about 1–2 months earlier than that suggested in Li (1997). The reason for this difference needs to be further explored.

5. Understanding the uniqueness and sensitivity of the ENSO mode

a. Dynamical origins of the ENSO mode

Early studies on linear ENSO dynamics were dedicated to revealing how the free oceanic modes become unstable by air–sea coupling. The earliest attempts were performed under the fast-SST limit, in which the SSTA and surface wind stress anomaly were typically approximated to be in balance with the thermocline fluctuation (Lau 1981; McCreary and Anderson 1984; Philander et al. 1984; Hirst 1986; Rennick and Haney 1986). Cane et al. (1990) found that the ENSO mode under the fast-SST limit originates from the gravest ocean basin mode, which involves ocean wave propagation and reflection. Therefore, this type of ENSO mode is referred to as the wave-oscillator (WO) mode. Later, the significance of the ocean memory effect associated with thermodynamic processes was recognized by Neelin (1991), who proposed that pure surface layer dynamics leads to an ENSO-like oscillatory mode (i.e., coupled SST mode). Adopting a two-strip approximation of the CZ model, which resolves both simplified surface layer dynamics and ocean dynamics, Jin (1997b) suggested the existence of another ENSO prototype mode distinct from the WO mode. With increasing intensity of air–sea coupling, the leading stationary free SST mode merges with the stationary ocean discharge/recharge adjustment mode involving basin-scale mass redistribution between the equatorial and off-equatorial ocean. The merging of these two free modes eventually leads to an interannual coupled mode with stronger air–sea coupling. This coupled mode is named the recharge-oscillator (RO) mode following the terminology in Jin (1997a).

The above findings are obtained using idealized models in which aspects of physical processes are simplified. In this section, we revisit the interpretation of the ENSO mode in the more realistic RCZ by examining the relevance of the ENSO prototype modes (i.e., the WO mode and RO mode). A series of linear stability analyses with the dynamical coupling coefficient μ increasing from 0 to 1.5 with an increment of 0.05 are performed to trace the dynamical origin of the ENSO mode. We begin with investigating the contribution to the ENSO mode from the individual feedback processes following An and Jin (2001). To study the role of the thermocline feedback, the other two feedback processes are switched off by setting $\gamma_{TH} = 1$, $\gamma_{ZA} = 0$, and $\gamma_{EK} = 0$ in Eq. (1). Similarly, the nondimensional parameters are set at $\gamma_{TH} = 0$, $\gamma_{ZA} = 1$, and $\gamma_{EK} = 0$ ($\gamma_{TH} = 0$, $\gamma_{ZA} = 0$, and $\gamma_{EK} = 1$) to study the role of

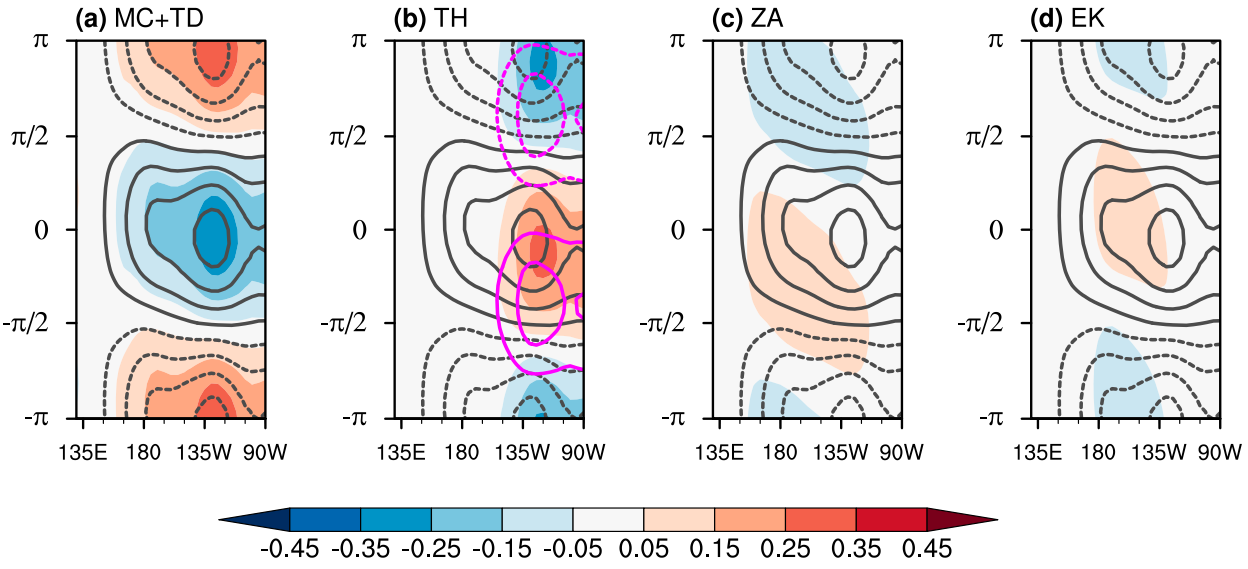

FIG. 6. Time evolution of equatorial SSTA (contour; °C) and heat budget terms (shaded; °C month^{-1}), including (a) summation of the mean advection of anomalous temperature and Newtonian cooling, (b) the thermocline feedback, (c) the zonal advective feedback, and (d) the Ekman feedback during a life cycle of the ENSO mode. The contour level for SSTA is 0.2°C, and dashed contours denote negative SSTA. In (b), the magenta contour denotes the thermocline feedback associated with the zonal mean component of the thermocline fluctuation. The contour level is 0.05°C month^{-1}, and dashed contours denote negative SSTA tendency.

the zonal advective feedback (the Ekman feedback). Scatterplots of the growth rate and frequency of the eigenmodes with varying μ in these three settings are shown in Figs. 7a–c.

Not surprisingly, the eigenmodes become less stable (more unstable) with increasing μ. The RO mode is favored by the thermocline feedback as it originates from the cluster of ocean discharge/recharge adjustment modes (Fig. 7a). The reason this RO mode does not originate from the stationary uncoupled modes as suggested in Jin (1997b) and An and Jin (2001) is that the two-dimensional ocean dynamics model in RCZ allows the full spectrum of uncoupled discharge/recharge adjustment modes, rather than only the stationary mode, to be resolved. In fact, Neelin and Jin (1993) found that the uncoupled SST mode can merge with any of the ocean discharge/recharge adjustment modes within the full spectrum to yield a RO mode. With the default value of dynamical coupling intensity (i.e., $\mu = 1$), the thermocline feedback-dominated RO mode exhibits a period of about 5 years. The associated SSTAs experience eastward propagation with maximum SSTA located in the eastern Pacific (Fig. 8a). A basin-scale equatorial thermocline deepening (shoaling) can be identified prior to the peak of El Niño (La Niña), suggesting the effect of the ocean heat content discharge/recharge process for the turnabout of the RO mode.

The zonal advective feedback, on the other hand, favors a WO mode as the corresponding coupled mode originates from the gravest ocean basin mode (Fig. 7b). As both the anomalous zonal current associated with the gravest ocean basin mode and background zonal temperature gradient peak in the central Pacific, the zonal advective feedback can efficiently excite a high-frequency mode with a period of about 1 year. How this near-annual mode contributes to or interacts with the annual cycle is an interesting topic and deserves further study. The connection between the zonal advective feedback and this near-annual mode can also be understood from the perspective that the ocean current response is more effectively excited with a high-frequency (e.g., near annual) wind stress forcing (An 2005). The Ekman feedback–induced mode is essentially a fast coupled SST mode by observing the similarity between the eigenmodes shown in Fig. 7c and those obtained under the fast-wave limit (not shown). For any prescribed dynamical coupling intensity, the growth rate of the Ekman feedback–induced mode is much smaller than that of the other two feedbacks induced modes, thus confirming the secondary role played by the Ekman feedback compared with the other two feedback processes. The zonal advective feedback–induced mode and Ekman feedback–induced mode both exhibit a westward SSTA propagation and maximum SSTA in the central Pacific (Figs. 8b,c). The discharge/recharge process is less effective for these two modes than that for the RO mode as evidenced by a lack of basin-scale equatorial thermocline fluctuations.

In a more realistic situation where all the thermodynamic feedback processes are active, the origin of the ENSO mode, although difficult to trace to a specific mode as above, can be speculated to root in the merge of the uncoupled SST mode and ocean discharge/recharge adjustment mode (Fig. 7d). Compared to the thermocline feedback–dominated mode, this ENSO mode is of higher frequency as the zonal advection feedback is taking effect. Note that, as found in An and Jin (2001), the ENSO mode identified with both the thermocline and zonal advective feedbacks being active may also originate from the gravest ocean basin mode. However, with stronger coupling intensity, the originally WO mode–like ENSO mode

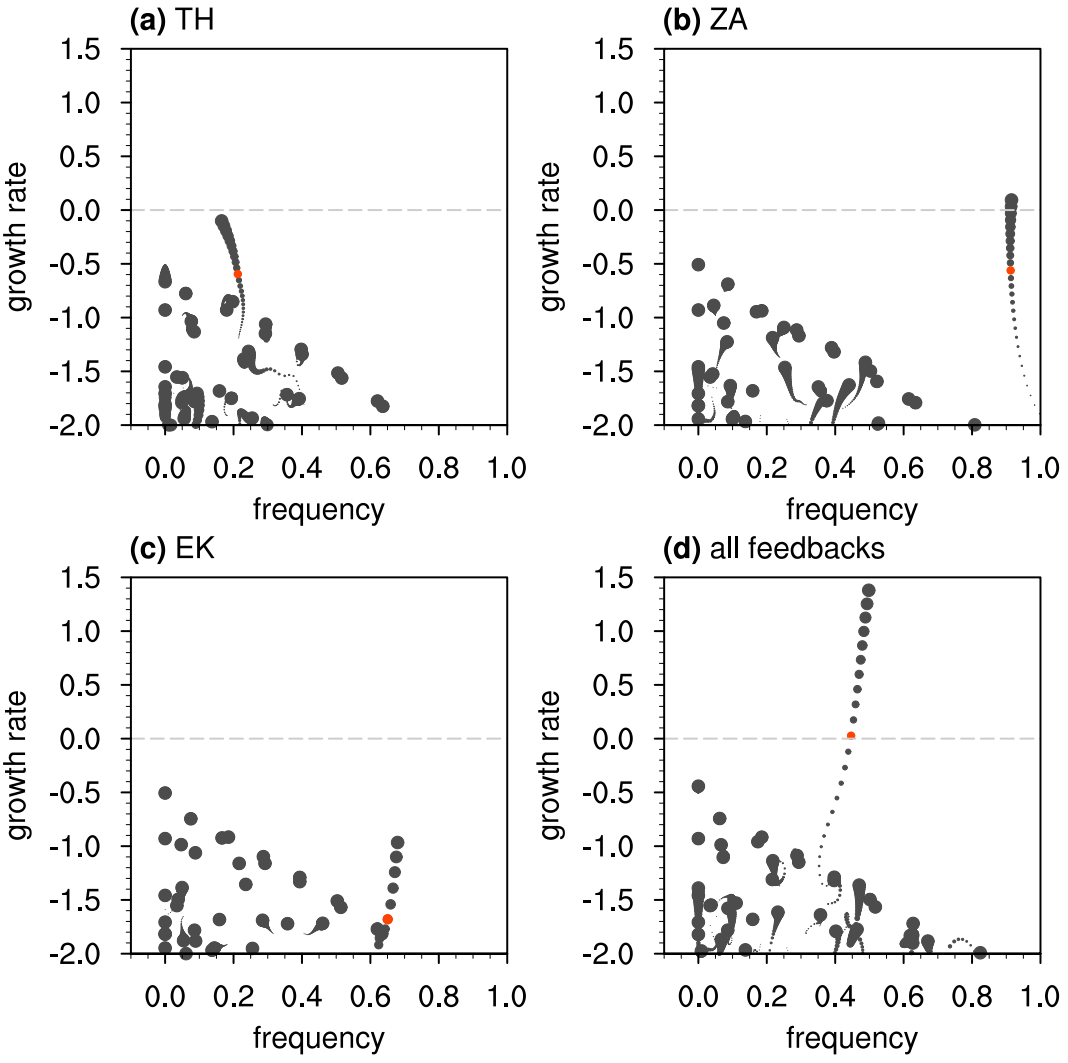

FIG. 7. Growth rate (yr^{-1}) and frequency (yr^{-1}) of RCZ's eigenmodes obtained in the situation where the (a) thermocline feedback, (b) zonal advective feedback, and (c) Ekman feedback is the single active feedback process. The increasing size of the dots represents a stronger dynamical coupling coefficient ranging from 0 to 1.5 with an increment of 0.05. (d) As in (a)–(c), but with all three feedback processes being active. The red dots in each figure denote the ENSO mode identified with the dynamical coupling coefficient equal to 1 with the exception of (c), where it is 1.25.

has a smaller frequency and becomes more RO mode–like. This changing behavior of the ENSO mode with stronger coupling intensity has also been found in An (2005) and is arguably attributed to the changing relative importance of the thermocline feedback and zonal advective feedback. The above results indicate that, away from the weak coupling end, the ENSO mode features mixed characteristics of the pure RO and WO modes, no matter its uncoupled origin. Thus, we refer to the ENSO mode in realistic situations where all feedback processes are involved as a generalized RO mode, considering that its dynamics can be depicted by the extended recharge–oscillator framework (Jin et al. 2020). As will be discussed later, this ENSO mode exhibits strong sensitivity to feedback intensities. It can be more RO mode–like, more WO mode–like, or a combination of both depending on different relative contributions from the thermocline feedback and the zonal advective feedback. This result is consistent with what has been found in An and Jin (2000, 2001). The RO mode (WO mode) away from the weak coupling end may exhibit characteristics not quite like the pure RO (WO) mode, but it will still be referred to as the RO-like (WO-like) ENSO mode in subsequent analyses.

b. Competition between the RO mode and WO mode

In the previous section, we showed that the thermocline feedback and zonal advective feedback favor the RO mode and WO mode, respectively. So why do we not have two leading ENSO modes when both feedback processes are active? To answer this question, we perform two series of linear stability analyses, in which either one of the two nondimensional

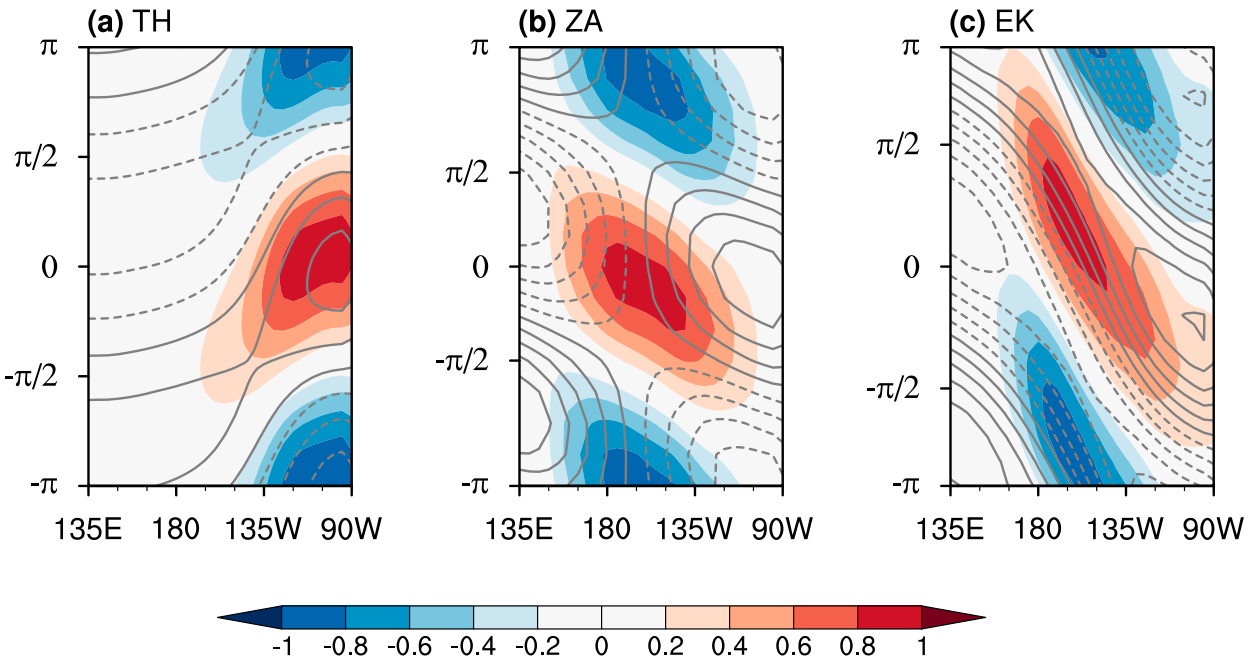

FIG. 8. Time evolution of the equatorial SSTA (shaded; °C) and thermocline fluctuation (contour; m) of the ENSO mode obtained in the situation where the (a) thermocline feedback, (b) zonal advective feedback, and (c) Ekman feedback is the single active feedback process. The ENSO mode is identified with the dynamical coupling coefficient equal to 1 in (a) and (b) and 1.25 in (c). The contour level for thermocline fluctuation is 4 m, and dashed contours denote shoaling of the thermocline.

parameters controlling intensities of the two feedbacks (i.e., γ_{TH} and γ_{ZA}) is fixed to be 1, and the other varies from 0 to 2 with an increment of 0.1. The dynamical coupling intensity is fixed at its default value of 1, and γ_{EK} is set to 0. Scatterplots of the growth rate and frequency associated with the eigenmodes in these two cases are shown in Fig. 9. In the former case with fixed γ_{ZA} and varying γ_{TH}, the first coupled mode at the small end of γ_{TH} is of high frequency (about 0.9 yr^{-1}), suggesting it as a WO mode. With increasing γ_{TH}, this WO mode exhibits smaller frequency and, more importantly, larger negative growth rate. Meanwhile, another mode with a lower frequency (i.e., the RO mode) emerges and gradually becomes less stable at the cost of the WO mode. Eventually, as γ_{TH} further increases to larger than 0.8, the order of the RO mode and WO mode switches, with the former becoming the first coupled mode. In the second case with fixed γ_{TH} and varying γ_{ZA}, the RO mode is the predominant mode at the weak end of γ_{ZA}. Its frequency monotonically increases with larger γ_{ZA} Upon the emergence of the WO mode as γ_{ZA} further increases, the RO mode becomes more stable and eventually gives its way to the increasingly unstable WO mode at γ_{ZA} larger than 1.7. Similar ENSO mode behavior is also identified in Fig. 1b. In that analysis, the warm pool–cold tongue SST contrast becomes larger with stronger mean wind stress intensity, resulting in stronger zonal advective feedback. Correspondingly, the growth rate of the RO (WO) mode decreases (increases). The above findings demonstrate that the RO mode and WO mode compete for predominance in shaping the ENSO mode depending on the relative intensity of the thermocline feedback and zonal advective feedback. The competition between the RO and WO modes determines the uniqueness of the ENSO mode. Although these two ENSO prototype modes may coexist with certain climate conditions in the parameter space, under no circumstances can they both become the leading mode. Another biproduct of such competition is the strong sensitivity of the ENSO mode. As a generalized RO mode exhibiting mixed characteristics of the RO and WO modes, the ENSO mode continuously shifts from being more WO mode–like (RO mode–like) toward more RO mode–like (WO mode–like) with stronger thermocline (zonal advective) feedback.

How the thermocline feedback and zonal advective feedback control the relevance of the two ENSO prototypes modes and eventually determine the uniqueness and sensitivity of the ENSO mode is further examined in a broad two-dimensional parameter space in which γ_{TH} and γ_{ZA} individually vary from 0.5 to 1.5 with an increment of 0.05. Considering that the Ekman feedback-induced mode bears similar spatio-temporal characteristics to the zonal advective feedback-induced mode, γ_{EK} is set to synchronously varies with γ_{ZA}. The growth rate of the first coupled mode, or the ENSO mode, is shown in Fig. 10a. An interesting feature is that the growth rate of the ENSO mode varies with γ_{TH} or γ_{ZA} in a nonmonotonic manner. For instance, with fixed γ_{ZA} at 1 and increasing γ_{TH} from 0.5 to 1.5, the growth rate of the ENSO mode first decreases, then increases, and gradually turns positive. A similar case is observed with fixed γ_{TH} smaller than 0.8 and increasing γ_{ZA}. Also, note that there is a second coupled mode near the neighborhood where the ENSO mode sees a local minimum in its growth rate along a fixed γ_{ZA} or γ_{TH}

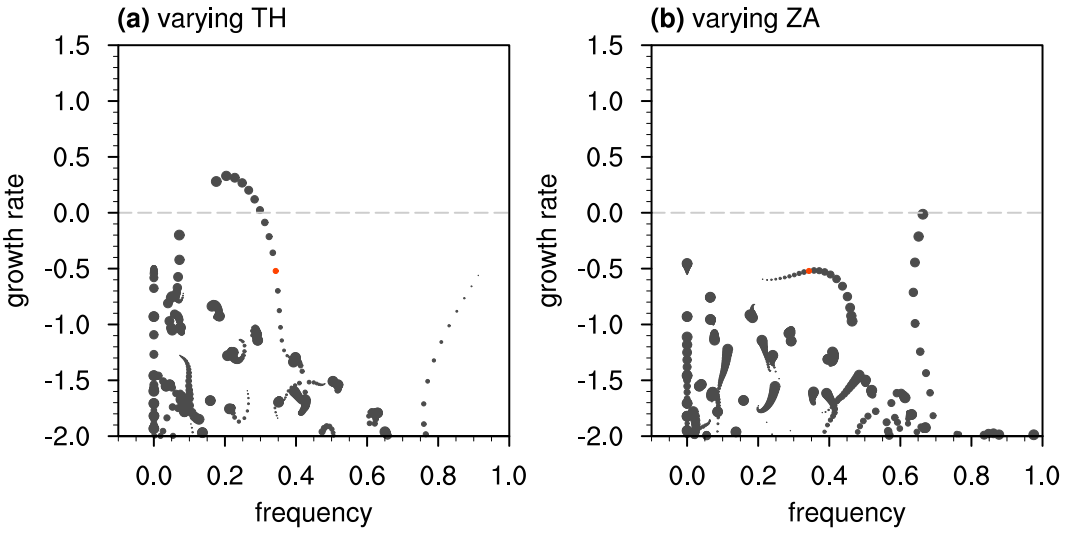

FIG. 9. (a) Growth rate (yr^{-1}) and frequency (yr^{-1}) of RCZ's eigenmodes with varying intensities of the thermocline feedback. Larger dots denote a stronger thermocline feedback intensity ranging from 0 to 2 with an increment of 0.1. (b) As in (a), but for the eigenmodes with varying intensities of the zonal advective feedback. The red dots in (a) and (b) denote the leading modes obtained with the intensity of the thermocline feedback and zonal advective feedback being 1, respectively.

(Fig. 10b). Both the ENSO mode and second coupled mode near this neighborhood are strongly stable, and their growth rates are close to each other. From the findings obtained in Fig. 9, we can speculate that these two modes correspond to the RO mode and WO mode, respectively; and the switch of order between them may result in the nonmonotonic change of the ENSO mode's growth rate with varying γ_{TH} or γ_{ZA}. For a clearer illustration of this speculation, Fig. 11 shows how the ENSO mode's spatiotemporal characteristics depend on γ_{TH} and γ_{ZA}. Generally, the ENSO mode exhibits a lower (higher) frequency with stronger (weaker) thermocline feedback and weaker (stronger) zonal advective feedback (Fig. 11a). The dependence of the ENSO mode's spatial pattern, depicted by the centroid longitude of SSTA at the peak phase, bears a strong resemblance to that of the frequency (Fig. 11b). Here, the centroid longitude of SSTA is defined as $\lambda_c = \int_{\lambda_W}^{\lambda_E} \lambda T_e \, d\lambda / \int_{\lambda_W}^{\lambda_E} T_e \, d\lambda$ where λ is the longitude, T_e is equatorial SSTA, λ_W = 140°E, and λ_E = 90°W. Only positive T_e, which dominates within the equatorial tropical Pacific during the warm peak phase of ENSO, is utilized to calculate λ_c. Lower (higher) frequency of the ENSO mode is associated with a more eastward (westward) SSTA center. The dependence of the ENSO mode's frequency and SSTA centroid longitude on γ_{TH} and γ_{ZA} is consistent with that found in the previous subsection and earlier studies (e.g., An and Jin 2000, 2001). Note that both the ENSO mode's frequency and SSTA

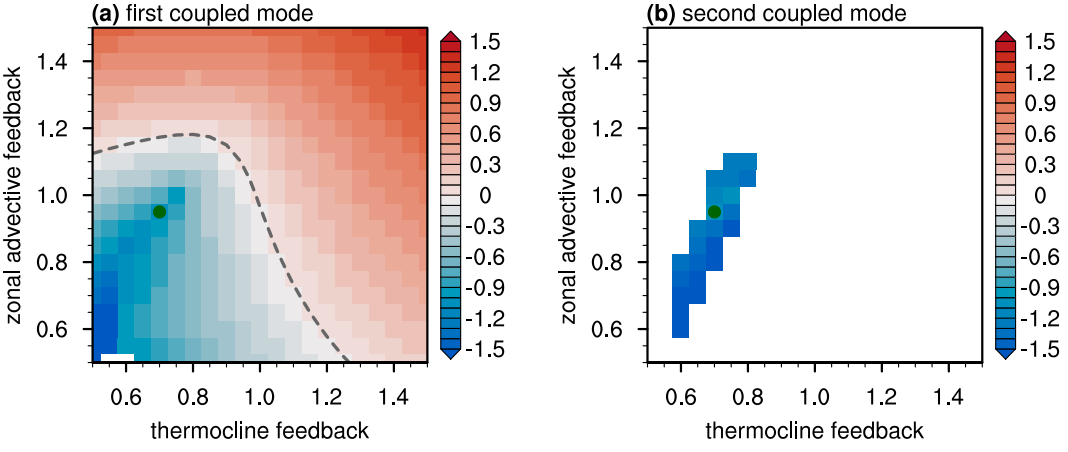

FIG. 10. Dependence of the growth rate (yr^{-1}) of the (a) first coupled mode and (b) second coupled mode on intensities of the thermocline feedback and zonal advective feedback. The modes that are not distinguishable from the uncoupled modes are blanked. The dashed curve in (a) denotes a zero-growth rate contour. The green dot in each figure marks the *D*-2 degeneracy point at which the RO and WO modes are closest to each other.

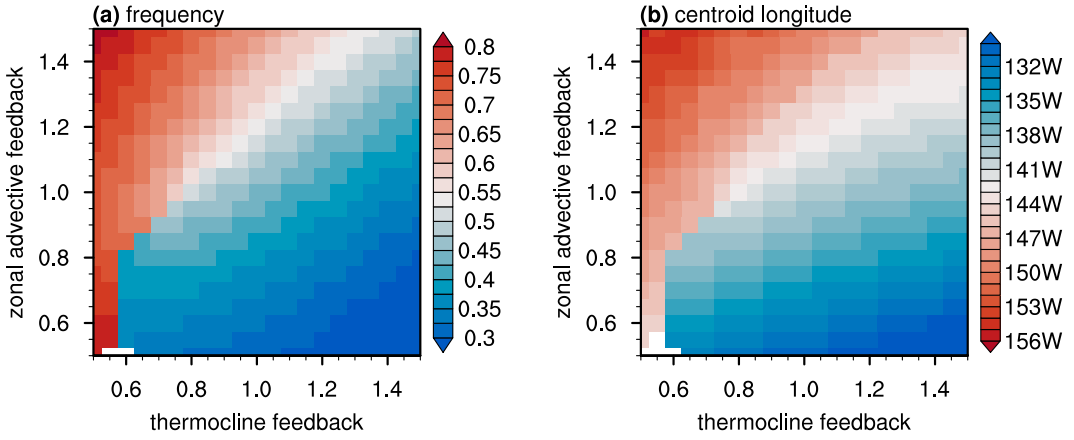

FIG. 11. Dependence of the (a) frequency (yr^{-1}) and (b) equatorial SSTA centroid longitude of the first coupled mode on the intensity of the thermocline feedback and zonal advective feedback.

centroid longitude exhibit a sharp contrast near the small end of γ_{TH} and γ_{ZA}, indicating the existence of two distinguished groups of ENSO modes (i.e., the RO mode and the WO mode). It is along the frequency boundary separating the two groups of ENSO modes where the minimum growth rate along each fixed γ_{TH} or γ_{ZA} is located. This finding confirms that the order of the RO and WO modes switches across the frequency boundary. Consistent with that indicated in Fig. 9, such a switch of order between the RO mode and the WO mode results in the nonmonotonic change of the ENSO mode's growth rate with increasing γ_{TH} or γ_{ZA}.

As shown in Figs. 1b and 9, the growth rate and frequency of one of the RO and WO modes tend to approach those of the other mode as these two modes switch order. In a two-dimensional space, there exists a point, the *D*-2 degeneracy point, at which these two modes coincide with each other. This *D*-2 degeneracy point, denoted by the green dot in Fig. 10, is identified by searching the point where the two ENSO prototype modes are closest to each other in the growth rate–frequency space. We further extend the search of the *D*-2 degeneracy point toward a three-dimensional parameter space by repeating the above analysis with various values of dynamical coupling intensity μ. The zero-growth rate contours and the *D*-2 degeneracy points for different choices of μ are shown in Fig. 12. With a weaker (stronger) coupling, the zero-growth rate contour shifts toward a stronger (weaker) thermocline feedback and zonal advective feedback. The growth rate and frequency at the *D*-2 degeneracy point are insensitive to μ, being about -1 and 0.55 yr^{-1} respectively. The fact that the *D*-2 degeneracy point is always in the far subcritical regime for whatever the value of μ further confirms that there cannot be two coexisting leading coupled modes for any climate condition in the parameter space.

6. Discussion

a. Relevance of the optimal growth mechanism

In recent years, a line of research has related the two types of El Niño to distinct precursors inside and outside of the tropical Pacific (Yu et al. 2010; Yu and Kim 2011; Ham et al. 2013a,b). Using the LIM approach, a new mechanism has been proposed where the two types of El Niño experience optimal growths from their respective optimal initial conditions (Newman et al. 2011a,b; Vimont et al. 2014, 2022; Capotondi and Sardeshmukh 2015). As discussed in the section 1, the effects of nonlinear and stochastic processes may have been

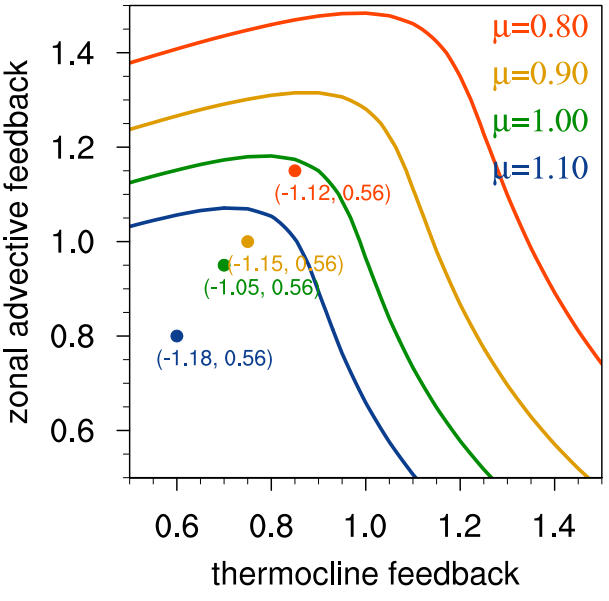

FIG. 12. ENSO mode's zero-growth rate contour in the two-dimensional thermocline feedback-zonal advective feedback intensity space. The ENSO mode has a negative (positive) growth rate to the left and bottom (right and top) of the zero-growth rate contour. Different colored contours represent varying dynamical coupling intensities. The dot with the same color as each contour denotes the corresponding *D*-2 degeneracy point. The growth rate (yr^{-1}) and frequency (yr^{-1}) associated with each *D*-2 degeneracy point are listed in the brackets below the dot. The first and second value in the parentheses denote the growth rate and frequency, respectively.

implicitly incorporated in the linear operator obtained with the data-driven LIM approach. Therefore, the relevance of optimal growth of normal modes should be interpreted cautiously. Newman et al. (2011a) attributed the optimal growth to the constructive and destructive interference between a 4- and a 2-yr stable eigenmode. However, this argument seems not supported by the present findings obtained within the CZ-type dynamical framework. With the observed basic state, the single leading ENSO mode far outstands all the other eigenmodes in terms of the growth rate. On the other hand, Vimont et al. (2022) found that the interference between a single ENSO mode and other Floquet modes associated with the annual cycle contributes to diverse evolutions of ENSO. It would be worthwhile to test this mechanism by analyzing the RCZ-derived linear operator with the seasonal cycle incorporated. It should also be noted that the Gill-type atmospheric component poses limits on RCZ's ability to capture the air–sea interaction processes out of the tropical Pacific. By further improving the model framework toward allowing more realistic interactions between the tropics and extratropics, RCZ may serve as a better tool to test the optimal growth mechanism.

b. *Relevance of the ENSO mode's sensitivity to ENSO diversity*

In the recent two decades, during which a La Niña–like mean state change is observed, CP El Niño is experiencing more frequent occurrences than before. This finding suggests that the ENSO flavor may be subject to low-frequency climate variabilities. Such modulation effect is confirmed in numerical studies (e.g., Yang et al. 2021; Chen et al. 2022) and is related to the ENSO mode's sensitivity to the mean state (e.g., An and Jin 2000; Fedorov and Philander 2000, 2001). A question then arises as to whether the low-frequency climate variability can explain ENSO diversity via its control of the ENSO mode properties.

In section 5, we demonstrated that the ENSO mode exhibits strong sensitivity in the parameter space spanned by varying intensities of the thermocline feedback and zonal advective feedback. This parameter space bears some resemblance to the basic state space constructed in Fedorov and Philander (2001) and Bejarano and Jin (2008) as the basic state's regulation of ENSO is realized through modulating the efficiency of dynamical and thermodynamic feedback processes. Therefore, our analysis in the parameter space provides a test bed to answer the question above. We performed a 200-yr linear stochastic simulation by time integration of the linear dynamical operator. The prescribed feedback intensities are subject to decadal variability, and the linear dynamical operator is instantaneously updated in accordance with the feedback intensities. The feedback intensities are picked according to the criteria that the growth rate of the ENSO mode is near $-0.1\ \mathrm{yr}^{-1}$. This is technically realized by searching the feedback intensities along the $-0.1\ \mathrm{yr}^{-1}$ contour in Fig. 10a. Such choices of feedback intensities allow the linear simulation to be sustained by stochastic forcing. The values of these feedback intensities, along with the corresponding ENSO mode's frequency and SSTA pattern, are shown in Fig. 13. With a stronger thermocline feedback intensity, the ENSO mode smoothly shifts from CP El Niño–like (i.e., with a high frequency and more westward-located SSTA) to EP El Niño–like (i.e., with a low frequency and more eastward-located SSTA). To mimic the decadal climate variability, the feedback intensities are randomly distributed along the $-0.1\ \mathrm{yr}^{-1}$ growth rate contour but are subject to an 11-yr running average. Stochastic forcing driving the model is in the form of WWB events as described in GJ22.

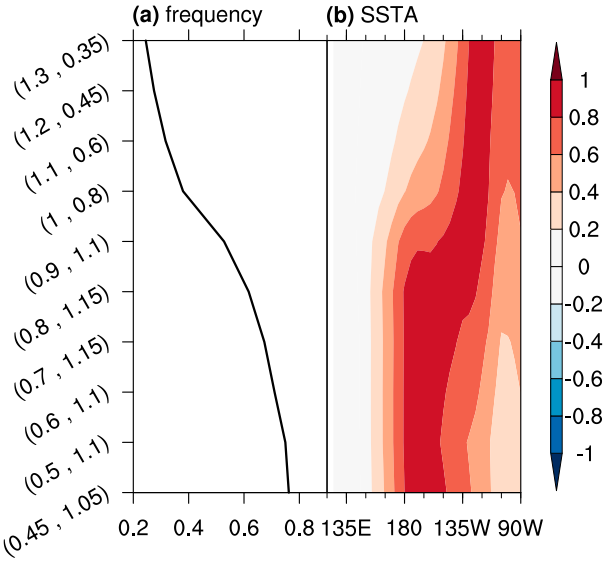

FIG. 13. (a) Frequency (yr^{-1}) and (b) equatorial SSTA at the warm peak phase (°C) associated with the ENSO mode identified with various sets of the thermocline feedback and zonal advective feedback intensities. The values of the feedback intensities are specified along the vertical axis. The first (second) value in each bracket denotes the intensity of the thermocline feedback (zonal advective feedback).

The prescribed thermocline feedback intensity and simulated equatorial SSTA during the last 50-yr simulation are shown in Fig. 14. Although the simulated ENSO shows interevent diversity, it exhibits a significant difference from the observed ENSO diversity. First, the simulated La Niña shows an SSTA center in either the central or eastern Pacific. This contrasts with the observed La Niña that exhibits little pattern diversity. Second, there is no existence of irregular alternance between EP and CP El Niño, which characterizes the observed ENSO diversity. Instead, within episodes when the thermocline feedback is relatively strong (e.g., years 10–20 or 38–50), there exists a single EP-type El Niño. Similarly, only a CP-type El Niño is observed within episodes with weak thermocline feedback. Therefore, it can be argued that the low-frequency climate variability is insufficient to explain ENSO diversity.

7. Summary

The fundamental mechanism for ENSO diversity has been a hot research topic, but no consensus has yet been reached. Previous studies by BXJ proposed a hypothesis based on pure linear dynamics by revealing that there are two coexisting

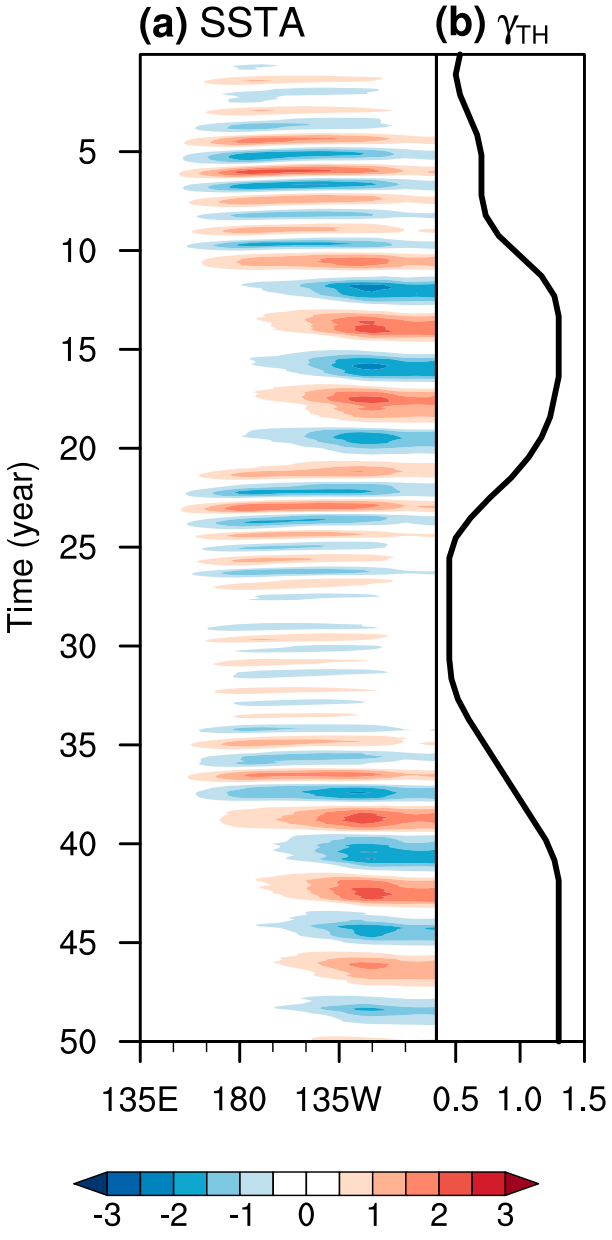

FIG. 14. (a) Fifty-year time evolution of equatorial SSTA (°C) in the linear stochastic simulation with decadal-varying feedback intensities. (b) Similar to (a), but for the prescribed thermocline feedback intensity.

ENSO-like eigenmodes of the CZ model under some climate conditions. These two modes exhibit spatiotemporal characteristics similar to the observed EP and CP El Niño and arguably can be randomly excited to lead to ENSO diversity. However, these two studies suffer from some errors in the calculation of the linear eigenmodes. Upon correcting these errors, there exists a single leading ENSO mode rather than two coexisting leading ENSO modes.

The uniqueness of the ENSO mode is confirmed in similar linear stability analysis using RCZ, a newly developed intermediate-coupled model capable of simulating ENSO diversity. With the observed annual mean basic state, the ENSO mode is near neutral and has a period of about 2 years. Several sets of linear stability analyses are performed in broad model parameter spaces to explore what determines the uniqueness of the ENSO mode. Consistent with suggestions in earlier theoretical studies, the ENSO mode may find its uncoupled ocean dynamics origin in either the ocean discharge/recharge adjustment mode or the gravest ocean basin mode. Corresponding to these two different origins, the ENSO mode is generally categorized as the RO mode and WO mode, with the pure thermocline feedback (zonal advective feedback) favoring the former (latter). In general situations where both feedback processes take effect, the ENSO mode can be interpreted as a generalized RO mode that exhibits mixed characteristics of the RO mode and WO mode. Depending on the relative intensity of the two feedback processes, the RO mode and WO mode compete for the dominant role in shaping the ENSO mode. It is such competition that contributes to the uniqueness of the ENSO mode. It also results in the strong sensitivity of the ENSO mode, which may be more RO (WO) mode-like when the thermocline feedback is more (less) dominant over the zonal advective feedback. The above results are consistent with previous findings in Jin and Neelin (1993), Jin (1997b), An and Jin (2001), and Fedorov and Philander (2001).

By observing that the ENSO mode predominates over other modes by a substantial degree, we argue that the two types of ENSO cannot be interpreted as two distinct oscillations excited by stochastic forcing. For the same reason, although the ENSO mode's strong sensitivity to the mean state may result in distinct preferred ENSO flavors in different epochs, it is insufficient to explain the coexisting two types of ENSO with irregular occurrences. However, the results above are obtained within the CZ-type framework and deserve further study to examine whether there could be more than one ENSO mode in a more complex framework, such as (i) including multiple vertical oceanic modes in the ocean dynamics model following Thual et al. (2011) and Zhao et al. (2021), (ii) extending the model domain toward the entire tropics, and (iii) improving the atmospheric component to better capture the relevant subtropical air–sea interaction processes. In addition, whether a seasonal-varying basic state allows more Floquet modes and whether these modes contribute to the nonmodal growth of ENSO as suggested in Vimont et al. (2022) needs to be further explored.

Although a single leading ENSO mode does not lead to ENSO diversity from a linear perspective, multiple ENSO flavors can be captured in long-term CZ-type model simulations (BXJ; Chen et al. 2015; Hayashi and Watanabe 2017; GJ22). We speculate that nonlinear processes resolved in these simulations play an essential role in ENSO diversity. A nonlinear pathway from a single leading ENSO mode toward the coexistence of two types of ENSO will be discussed in Part II.

Acknowledgments. This research was supported by the U.S. National Science Foundation (AGS-2219257). We thank

three anonymous reviewers for providing valuable comments and suggestions. Thanks also go to May Izumi for editing the manuscript. This is SOEST contribution 11725.

Data availability statement. The reanalysis data for deriving the model's basic state are openly available from the Asia-Pacific Data Research Center at http://apdrc.soest.hawaii.edu/data/data.php and from the NOAA Physical Sciences Laboratory at https://psl.noaa.gov/data/gridded/index.html. The model simulation data and derived data for analysis are available upon request to the corresponding author.

REFERENCES

An, S.-I., 2005: Relative roles of the equatorial upper ocean zonal current and thermocline in determining the timescale of the tropical climate system. *Theor. Appl. Climatol.*, **81**, 121–132, https://doi.org/10.1007/s00704-004-0105-0.

——, and F.-F. Jin, 2000: An eigen analysis of the interdecadal changes in the structure and frequency of ENSO mode. *Geophys. Res. Lett.*, **27**, 2573–2576, https://doi.org/10.1029/1999GL011090.

——, and ——, 2001: Collective role of zonal thermocline and zonal advective feedbacks in ENSO mode. *J. Climate*, **14**, 3421–3432, https://doi.org/10.1175/1520-0442(2001)014<3421:CROTAZ>2.0.CO;2.

Ashok, K., S. K. Behera, S. A. Rao, H. Weng, and T. Yamagata, 2007: El Niño Modoki and its possible teleconnection. *J. Geophys. Res.*, **112**, C11007, https://doi.org/10.1029/2006JC003798.

Battisti, D. S., and A. C. Hirst, 1989: Interannual variability in a tropical atmosphere–ocean model: Influence of the basic state, ocean geometry and nonlinearity. *J. Atmos. Sci.*, **46**, 1687–1712, https://doi.org/10.1175/1520-0469(1989)046<1687:IVIATA>2.0.CO;2.

Bayr, T., and M. Latif, 2023: ENSO atmospheric feedbacks under global warming and their relation to mean-state changes. *Climate Dyn.*, **60**, 2613–2631, https://doi.org/10.1007/s00382-022-06454-3.

Bejarano, L., and F.-F. Jin, 2008: Coexistence of equatorial coupled modes of ENSO. *J. Climate*, **21**, 3051–3067, https://doi.org/10.1175/2007JCLI1679.1.

Cane, M. A., M. Münnich, and S. F. Zebiak, 1990: A study of self-excited oscillations of the tropical ocean–atmosphere system. Part I: Linear analysis. *J. Atmos. Sci.*, **47**, 1562–1577, https://doi.org/10.1175/1520-0469(1990)047<1562:ASOSEO>2.0.CO;2.

Capotondi, A., 2013: ENSO diversity in the NCAR CCSM4 climate model. *J. Geophys. Res. Oceans*, **118**, 4755–4770, https://doi.org/10.1002/jgrc.20335.

——, and P. D. Sardeshmukh, 2015: Optimal precursors of different types of ENSO events. *Geophys. Res. Lett.*, **42**, 9952–9960, https://doi.org/10.1002/2015GL066171.

Chen, D., and Coauthors, 2015: Strong influence of westerly wind bursts on El Niño diversity. *Nat. Geosci.*, **8**, 339–345, https://doi.org/10.1038/ngeo2399.

Chen, N., and A. J. Majda, 2017: Simple stochastic dynamical models capturing the statistical diversity of El Niño Southern Oscillation. *Proc. Natl. Acad. Sci. USA*, **114**, 1468–1473, https://doi.org/10.1073/pnas.1620766114.

——, ——, and S. Thual, 2018: Observations and mechanisms of a simple stochastic dynamical model capturing El Niño diversity. *J. Climate*, **31**, 449–471, https://doi.org/10.1175/JCLI-D-16-0880.1.

——, X. Fang, and J.-Y. Yu, 2022: A multiscale model for El Niño complexity. *npj Climate Atmos. Sci.*, **5**, 16, https://doi.org/10.1038/s41612-022-00241-x.

Dommenget, D., T. Bayr, and C. Frauen, 2013: Analysis of the non-linearity in the pattern and time evolution of El Niño Southern Oscillation. *Climate Dyn.*, **40**, 2825–2847, https://doi.org/10.1007/s00382-012-1475-0.

Fedorov, A. V., and S. G. Philander, 2000: Is El Niño changing? *Science*, **288**, 1997–2002, https://doi.org/10.1126/science.288.5473.1997.

——, and ——, 2001: A stability analysis of tropical ocean–atmosphere interactions: Bridging measurements and theory for El Niño. *J. Climate*, **14**, 3086–3101, https://doi.org/10.1175/1520-0442(2001)014<3086:ASAOTO>2.0.CO;2.

——, S. Hu, M. Lengaigne, and E. Guilyardi, 2015: The impact of westerly wind bursts and ocean initial state on the development, and diversity of El Niño events. *Climate Dyn.*, **44**, 1381–1401, https://doi.org/10.1007/s00382-014-2126-4.

Geng, L., and F.-F. Jin, 2022: ENSO diversity simulated in a revised Cane-Zebiak model. *Front. Earth Sci.*, **10**, 899323, https://doi.org/10.3389/feart.2022.899323.

——, and ——, 2023: Insights into ENSO diversity from an intermediate coupled model. Part II: Role of nonlinear dynamics and stochastic forcing. *J. Climate*, **36**, 7527–7547, https://doi.org/10.1175/JCLI-D-23-0044.1.

Giese, B. S., and S. Ray, 2011: El Niño variability in simple ocean data assimilation (SODA), 1871–2008. *J. Geophys. Res.*, **116**, C02024, https://doi.org/10.1029/2010JC006695.

Ham, Y.-G., J.-S. Kug, and J.-Y. Park, 2013a: Two distinct roles of Atlantic SSTs in ENSO variability: North tropical Atlantic SST and Atlantic Niño. *Geophys. Res. Lett.*, **40**, 4012–4017, https://doi.org/10.1002/grl.50729.

——, ——, ——, and F.-F. Jin, 2013b: Sea surface temperature in the north tropical Atlantic as a trigger for El Niño/southern oscillation events. *Nat. Geosci.*, **6**, 112–116, https://doi.org/10.1038/ngeo1686.

Hayashi, M., and M. Watanabe, 2017: ENSO complexity induced by state dependence of westerly wind events. *J. Climate*, **30**, 3401–3420, https://doi.org/10.1175/JCLI-D-16-0406.1.

Hirst, A. C., 1986: Unstable and damped equatorial modes in simple coupled ocean-atmosphere models. *J. Atmos. Sci.*, **43**, 606–632, https://doi.org/10.1175/1520-0469(1986)043<0606:UADEMI>2.0.CO;2.

Hu, S., and A. V. Fedorov, 2019: The extreme El Niño of 2015–2016: The role of westerly and easterly wind bursts, and preconditioning by the failed 2014 event. *Climate Dyn.*, **52**, 7339–7357, https://doi.org/10.1007/s00382-017-3531-2.

Jadhav, J., S. Panickal, S. Marathe, and K. Ashok, 2015: On the possible cause of distinct El Niño types in the recent decades. *Sci. Rep.*, **5**, 17009, https://doi.org/10.1038/srep17009.

Jin, F.-F., 1997a: An equatorial ocean recharge paradigm for ENSO. Part I: Conceptual model. *J. Atmos. Sci.*, **54**, 811–829, https://doi.org/10.1175/1520-0469(1997)054<0811:AEORPF>2.0.CO;2.

——, 1997b: An equatorial ocean recharge paradigm for ENSO. Part II: A stripped-down coupled model. *J. Atmos. Sci.*, **54**, 830–847, https://doi.org/10.1175/1520-0469(1997)054<0830:AEORPF>2.0.CO;2.

——, and J. D. Neelin, 1993: Modes of interannual tropical ocean–atmosphere interaction—A unified view. Part I: Numerical

results. *J. Atmos. Sci.*, **50**, 3477–3503, https://doi.org/10.1175/1520-0469(1993)050<3477:MOITOI>2.0.CO;2.

——, H.-C. Chen, S. Zhao, M. Hayashi, C. Karamperidou, M. F. Stuecker, R. Xie, and L. Geng, 2020: Simple ENSO models. *El Niño Southern Oscillation in a Changing Climate*, *Geophys. Monogr.*, Vol. 253, Amer. Geophys. Union, 119–151, https://doi.org/10.1002/9781119548164.ch6.

Johnson, N. C., 2013: How many ENSO flavors can we distinguish? *J. Climate*, **26**, 4816–4827, https://doi.org/10.1175/JCLI-D-12-00649.1.

Kao, H.-Y., and J.-Y. Yu, 2009: Contrasting eastern-Pacific and central-Pacific types of ENSO. *J. Climate*, **22**, 615–632, https://doi.org/10.1175/2008JCLI2309.1.

Kug, J.-S., and Y.-G. Ham, 2011: Are there two types of La Niña? *Geophys. Res. Lett.*, **38**, L16704, https://doi.org/10.1029/2011GL048237.

——, F.-F. Jin, and S.-I. An, 2009: Two types of El Niño events: Cold tongue El Niño and warm pool El Niño. *J. Climate*, **22**, 1499–1515, https://doi.org/10.1175/2008JCLI2624.1.

——, J. Choi, S.-I. An, F.-F. Jin, and A. T. Wittenberg, 2010: Warm pool and cold tongue El Niño events as simulated by the GFDL 2.1 coupled GCM. *J. Climate*, **23**, 1226–1239, https://doi.org/10.1175/2009JCLI3293.1.

Larkin, N. K., and D. E. Harrison, 2005: Global seasonal temperature and precipitation anomalies during El Niño autumn and winter. *Geophys. Res. Lett.*, **32**, L16705, https://doi.org/10.1029/2005GL022860.

Lau, K.-M., 1981: Oscillations in a simple equatorial climate system. *J. Atmos. Sci.*, **38**, 248–261, https://doi.org/10.1175/1520-0469(1981)038<0248:OIASEC>2.0.CO;2.

Li, T., 1997: Phase transition of the El Niño–Southern Oscillation: A stationary SST mode. *J. Atmos. Sci.*, **54**, 2872–2887, https://doi.org/10.1175/1520-0469(1997)054<2872:PTOTEN>2.0.CO;2.

Lian, T., D. Chen, Y. Tang, and Q. Wu, 2014: Effects of westerly wind bursts on El Niño: A new perspective. *Geophys. Res. Lett.*, **41**, 3522–3527, https://doi.org/10.1002/2014GL059989.

McCreary, J. P., Jr., and D. L. T. Anderson, 1984: A simple model of El Niño and the Southern Oscillation. *Mon. Wea. Rev.*, **112**, 934–946, https://doi.org/10.1175/1520-0493(1984)112<0934:ASMOEN>2.0.CO;2.

McPhaden, M. J., 2012: A 21st century shift in the relationship between ENSO SST and warm water volume anomalies. *Geophys. Res. Lett.*, **39**, L09706, https://doi.org/10.1029/2012GL051826.

Meinen, C. S., and M. J. McPhaden, 2000: Observations of warm water volume changes in the equatorial Pacific and their relationship to El Niño and La Niña. *J. Climate*, **13**, 3551–3559, https://doi.org/10.1175/1520-0442(2000)013<3551:OOWWVC>2.0.CO;2.

Neelin, J. D., 1991: The slow sea surface temperature mode and the fast-wave limit: Analytic theory for tropical interannual oscillations and experiments in a hybrid coupled model. *J. Atmos. Sci.*, **48**, 584–606, https://doi.org/10.1175/1520-0469(1991)048<0584:TSSSTM>2.0.CO;2.

——, and F.-F. Jin, 1993: Modes of interannual tropical ocean–atmosphere interaction—A unified view. Part II: Analytical results in the weak-coupling limit. *J. Atmos. Sci.*, **50**, 3504–3522, https://doi.org/10.1175/1520-0469(1993)050<3504:MOITOI>2.0.CO;2.

Newman, M., M. A. Alexander, and J. D. Scott, 2011a: An empirical model of tropical ocean dynamics. *Climate Dyn.*, **37**, 1823–1841, https://doi.org/10.1007/s00382-011-1034-0.

——, S.-I. Shin, and M. A. Alexander, 2011b: Natural variation in ENSO flavors. *Geophys. Res. Lett.*, **38**, L14705, https://doi.org/10.1029/2011GL047658.

Okumura, Y. M., 2019: ENSO diversity from an atmospheric perspective. *Curr. Climate Change Rep.*, **5**, 245–257, https://doi.org/10.1007/s40641-019-00138-7.

Philander, S. G. H., T. Yamagata, and R. C. Pacanowski, 1984: Unstable air–sea interactions in the tropics. *J. Atmos. Sci.*, **41**, 604–613, https://doi.org/10.1175/1520-0469(1984)041<0604:UASIIT>2.0.CO;2.

Ren, H.-L., and F.-F. Jin, 2013: Recharge oscillator mechanisms in two types of ENSO. *J. Climate*, **26**, 6506–6523, https://doi.org/10.1175/JCLI-D-12-00601.1.

Rennick, M. A., and R. L. Haney, 1986: Stable and unstable air–sea interactions in the equatorial region. *J. Atmos. Sci.*, **43**, 2937–2943, https://doi.org/10.1175/1520-0469(1986)043<2937:SAUASI>2.0.CO;2.

Shin, S.-I., P. D. Sardeshmukh, M. Newman, C. Penland, and M. A. Alexander, 2021: Impact of annual cycle on ENSO variability and predictability. *J. Climate*, **34**, 171–193, https://doi.org/10.1175/JCLI-D-20-0291.1.

Takahashi, K., and B. Dewitte, 2016: Strong and moderate nonlinear El Niño regimes. *Climate Dyn.*, **46**, 1627–1645, https://doi.org/10.1007/s00382-015-2665-3.

——, A. Montecinos, K. Goubanova, and B. Dewitte, 2011: ENSO regimes: Reinterpreting the canonical and Modoki El Niño. *Geophys. Res. Lett.*, **38**, L10704, https://doi.org/10.1029/2011GL047364.

Taschetto, A. S., A. S. Gupta, N. C. Jourdain, A. Santoso, C. C. Ummenhofer, and M. H. England, 2014: Cold tongue and warm pool ENSO events in CMIP5: Mean state and future projections. *J. Climate*, **27**, 2861–2885, https://doi.org/10.1175/JCLI-D-13-00437.1.

Thual, S., B. Dewitte, S.-I. An, and N. Ayoub, 2011: Sensitivity of ENSO to stratification in a recharge–discharge conceptual model. *J. Climate*, **24**, 4332–4349, https://doi.org/10.1175/2011JCLI4148.1.

Vimont, D. J., M. A. Alexander, and M. Newman, 2014: Optimal growth of central and East Pacific ENSO events. *Geophys. Res. Lett.*, **41**, 4027–4034, https://doi.org/10.1002/2014GL059997.

——, M. Newman, D. S. Battisti, and S.-I. Shin, 2022: The role of seasonality and the ENSO mode in central and east Pacific ENSO growth and evolution. *J. Climate*, **35**, 3195–3209, https://doi.org/10.1175/JCLI-D-21-0599.1.

Wakata, Y., and E. S. Sarachik, 1991: Unstable coupled atmosphere–ocean basin modes in the presence of a spatially varying basic state. *J. Atmos. Sci.*, **48**, 2060–2077, https://doi.org/10.1175/1520-0469(1991)048<2060:UCABMI>2.0.CO;2.

Williams, I. N., and C. M. Patricola, 2018: Diversity of ENSO events unified by convective threshold sea surface temperature: A nonlinear ENSO index. *Geophys. Res. Lett.*, **45**, 9236–9244, https://doi.org/10.1029/2018GL079203.

Xie, R., and F.-F. Jin, 2018: Two leading ENSO modes and El Niño types in the Zebiak–Cane model. *J. Climate*, **31**, 1943–1962, https://doi.org/10.1175/JCLI-D-17-0469.1.

Yang, Q., A. J. Majda, and N. Chen, 2021: ENSO diversity in a tropical stochastic skeleton model for the MJO, El Niño, and dynamic Walker circulation. *J. Climate*, **34**, 3481–3501, https://doi.org/10.1175/JCLI-D-20-0447.1.

Yeh, S.-W., J.-S. Kug, B. Dewitte, M.-H. Kwon, B. P. Kirtman, and F.-F. Jin, 2009: El Niño in a changing climate. *Nature*, **461**, 511–514, https://doi.org/10.1038/nature08316.

Yu, J.-Y., and S. T. Kim, 2011: Relationships between extratropical sea level pressure variations and the central Pacific and eastern Pacific types of ENSO. *J. Climate*, **24**, 708–720, https://doi.org/10.1175/2010JCLI3688.1.

——, H.-Y. Kao, and T. Lee, 2010: Subtropics-related interannual sea surface temperature variability in the central equatorial Pacific. *J. Climate*, **23**, 2869–2884, https://doi.org/10.1175/2010JCLI3171.1.

Zebiak, S. E., and M. A. Cane, 1987: A model El Niño–Southern Oscillation. *Mon. Wea. Rev.*, **115**, 2262–2278, https://doi.org/10.1175/1520-0493(1987)115<2262:AMENO>2.0.CO;2.

Zhao, S., F.-F. Jin, X. Long, and M. A. Cane, 2021: On the breakdown of ENSO's relationship with thermocline depth in the central-equatorial Pacific. *Geophys. Res. Lett.*, **48**, e2020GL092335, https://doi.org/10.1029/2020GL092335.